The amplitude of the kilohertz quasi-periodic oscillations in 4U 1636-53 in the frequency-energy space

Ribeiro, Evandro M.; Méndez, Mariano; Avellar, Marcio G. B. de; Zhang, Guobao; Karpouzas, Konstantinos

Published in:
Monthly Notices of the Royal Astronomical Society

DOI:
10.1093/mnras/stz2463

Publication date:
2019

Monthly Notices
of the
ROYAL ASTRONOMICAL SOCIETY

MNRAS **489,** 4980–4991 (2019)
Advance Access publication 2019 September 5

doi:10.1093/mnras/stz2463

The amplitude of the kilohertz quasi-periodic oscillations in 4U 1636−53 in the frequency-energy space

Evandro M. Ribeiro [1]★ Mariano Méndez,[1] Marcio G. B. de Avellar,[2] Guobao Zhang[3,4] and Konstantinos Karpouzas[1,5]

[1]*Kapteyn Astronomical Institute, University of Groningen, PO BOX 800, NL-9700 AV Groningen, the Netherlands*
[2]*Instituto Tecnológico de Aeronáutica, ITA, 1228-900, SP, Brazil*
[3]*Yunnan Observatories, Chinese Academy of Sciences (CAS), Kunming 650216, P.R. China*
[4]*Key Laboratory for the Structure and Evolution of Celestial Objects, CAS, Kunming 650216, P.R. China*
[5]*School of Physics and Astronomy, University of Southampton, Southampton, SO17 1BJ, UK.*

Accepted 2019 August 24. Received 2019 August 22; in original form 2019 May 21

ABSTRACT

We present for the neutron-star low-mass X-ray binary 4U 1636−53, and for the first time for any source of kilohertz quasi-periodic oscillations (kHz QPOs), the two-dimensional behaviour of the fractional rms amplitude of the kHz QPOs in the parameter space defined by QPO frequency and photon energy. We find that the rms amplitude of the lower kHz QPO increases with energy up to ∼12 keV and then decreases at higher energies, while the rms amplitude of the upper kHz QPO either continues increasing or levels off at high energies. The rms amplitude of the lower kHz QPO increases and then decreases with frequency, peaking at ∼760 Hz, while the amplitude of the upper kHz QPO decreases with frequency, with a local maximum at around ∼770 Hz, and is consistent with becoming zero at the same QPO frequency, ∼1400 Hz, in all energy bands, thus constraining the neutron-star mass at $M_{NS} \leq 1.6\,\mathrm{M}_{\odot}$, under the assumption that this QPO reflects the Keplerian frequency at the inner edge of the accretion disc. We show that the slope of the rms energy spectrum is connected to the changing properties of the kHz QPOs in different energy bands as its frequencies change. Finally, we discuss a possible mechanism responsible for the radiative properties of the kHz QPOs and, based on a model in which the QPO arises from oscillations in a Comptonizing cloud of hot electrons, we show that the properties of the kHz QPOs can constrain the thermodynamic properties of the inner accretion flow.

Key words: accretion, accretion discs – stars: individual: 4U 1636-53 – stars: neutron – X-rays: binaries.

1 INTRODUCTION

20 yr after the discovery of kilohertz quasi-periodic oscillations (kHz QPOs; Strohmayer et al. 1996; van der Klis et al. 1996) in neutron-star low-mass X-ray binaries (NS-LMXB), a satisfactory explanation of the origin of these QPOs remains a challenge (Gilfanov, Revnivtsev & Molkov 2003; Mendez 2006; Barret 2013; de Avellar et al. 2013; Peille, Barret & Uttley 2015; Cackett 2016; Wang 2016; Troyer et al. 2018). Both the timing and spectral properties of these high-frequency oscillations are likely driven by general relativistic effects (Stella & Vietri 1998, 1999; Kato 2005), the neutron-star mass and radius (Miller, Lamb & Psaltis 1998), and the physical processes taking place in the inner regions of the accretion flow (Lee & Miller 1998; Lee, Misra & Taam 2001; Kumar & Misra 2014).

The kHz QPOs usually appear as a pair of peaks in the X-ray power-density spectrum (PDS) of NS-LMXB. The two components of the pair of kHz QPOs are called the lower and upper kHz QPO, respectively, according to their frequency. In those cases in which a single QPO is present in the PDS of an observation, the QPO can be identified by other properties such as their amplitude (Di Salvo et al. 2001; Mendez, van der Klis & Ford 2001), quality factor $Q = \nu_0/\mathrm{FWHM}$, where ν_0 is the QPO frequency and FWHM is the full width at half maximum of the profile of the QPO (Barret, Olive & Miller 2006), the relation between the QPO frequencies and the spectral state of the NS-LMXB (Mendez et al. 1998b), or the time lags of the QPOs (Barret 2013; de Avellar et al. 2013; Peille et al. 2015; de Avellar et al. 2016; Troyer et al. 2018). For instance, the upper kHz QPO has usually higher fractional rms amplitude and lower quality factor than the lower kHz QPO (e.g. Di Salvo

★ E-mail: ribeiro@astro.rug.nl

et al. 2001; van Straaten et al. 2002; Barret et al. 2006; Mendez 2006; Altamirano et al. 2008; Troyer et al. 2018), and is observed across different spectral states, whereas the lower kHz QPO is only observed in the intermediate state (e.g. Mendez et al. 1998b; Zhang et al. 2017a).

Several models have been put forward in order to explain the frequency of the kHz QPOs in LMXB, among those are the sonic-point model (Miller et al. 1998), the relativistic precession model (Stella & Vietri 1998), the two-oscillator model (Osherovich & Titarchuk 1999; Titarchuk 2003), the relativistic resonant model (Kluzniak & Abramowicz 2001), the deformed-disc oscillation model (Kato 2009; Mukhopadhyay 2009), and magnetohydrodynamic models (Zhang 2004; Li & Zhang 2005; Erkut, Psaltis & Alpar 2008; Shi & Li 2009; de Avellar et al. 2018). So far none of these models can satisfactorily explain all of the observed properties of the kHz QPOs (e.g. Lin et al. 2011; Wang 2016).

Another approach to understand the origin of the kHz QPOs is to investigate the relation between the properties of the QPOs and the X-ray flux and spectra, and to identify the radiative mechanism responsible for the QPOs. It is known that the frequencies of these oscillations depend on the spectral state of the source, which can be parametrized by the position of the source in the colour–colour diagram (Mendez et al. 1998b; Ribeiro et al. 2017; Zhang et al. 2017a). On the other hand, the fractional rms amplitude of the kHz QPOs increases with photon energy up to 10 keV (Berger et al. 1996; Zhang et al. 1996; Wijnands et al. 1997; Mendez et al. 2001; Gilfanov et al. 2003), and it may decrease at energies above ∼10 keV (Mukherjee & Bhattacharyya 2012). The time-averaged X-ray spectrum of NS-LMXBs is composed by a soft thermal component due to the neutron-star surface or boundary layer and the accretion disc and a hard component due to the inverse Compton scattering of soft thermal photons in a corona consisting of energetic electrons (Barret 2001; Lin, Remillard & Homan 2007). It is worth noticing that at energies above ∼10 keV the contribution of the soft thermal component to the total emission becomes insignificant, implying that the radiative mechanism responsible for the amplitude of the kHz QPOs must take place in the hard Comptonizing component (Gilfanov et al. 2003; Mendez 2006).

In previous studies of this source, Zhang et al. (2017a) explored the connection between the presence of the lower and upper kHz QPO and the spectral state of the source, and Ribeiro et al. (2017) studied the relation between the QPO properties and the spectral parameters. In this work we study the evolution of the fractional rms amplitude of the kHz QPOs in 4U 1636−53, both as a function of the QPO frequency and energy.

In this paper we combine data from the spectral and timing domain to reveal new information on the properties of the kHz QPOs in the NS-LMXB 4U 1636−53. This source shows a recurring ∼40 d cycle of spectral transitions (Belloni et al. 2007), making it an excellent target to study the changes of the properties of the kHz QPOs. 4U 1636−53 was observed 1576 times with the *Rossi X-ray Timing Explorer* (*RXTE*) satellite, providing an outstanding data set to carry out detailed analysis of the kHz QPO.

In Section 2 we explain the methods; in Section 3 we show our results; in Section 4 we discuss our findings and present our conclusions about the results of our novel approach.

2 METHODS

From the 1576 *RXTE* observations of the NS-LMXB 4U 1636−53, we selected those that were carried out in Event mode with a time

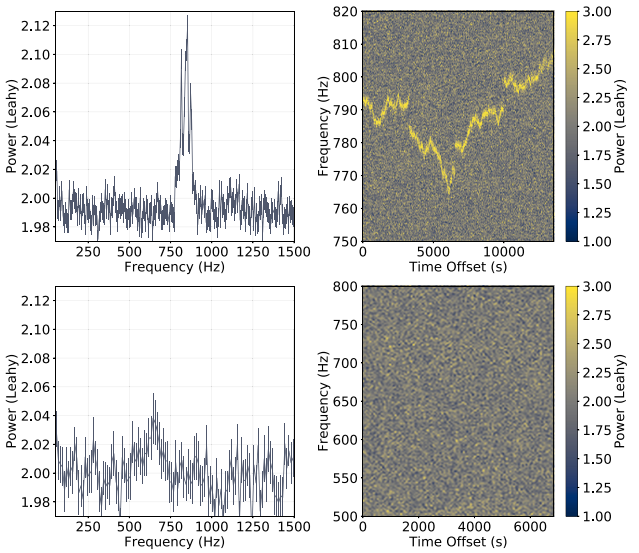

Figure 1. Example of two observations with a kHz QPO in 4U 1636−53. The left column shows the averaged power spectrum of the observation, and the right column shows the corresponding dynamical power spectrum. *Top row*: good quality observation, in which we are able to trace the QPO in each non-overlapping segment of 16 s. The multiple peak profile of the QPO in the left-hand panel is due to the change of the QPO frequency during the observation. The small gaps in the dynamical power spectrum, apparent as small jumps of the frequency of the QPO at around 2500, 7000, and 10 000 s, come from the selection of *Good Time Intervals*. *Bottom row*: worst case scenario, in which we are not able to identify the QPO in the dynamical power spectrum, but we are still able to detect the QPO in the averaged power spectrum. In this case we assigned a single frequency to the QPO for the entire observation.

resolution of at least 125 μs. We extracted power spectra of the selected observations using all PCA energy channels over 16 s segments with a Nyquist frequency of 2048 Hz. We discarded those 16 s segments in which there were telemetry drop-outs or an X-ray burst was present in the light curve, and we averaged the remaining 16 s power spectra to produce a single power spectrum per observation. We searched the average power spectrum of each observation for kHz QPOs at frequencies larger than 200 Hz. The criteria used to identify kHz QPOs were the same as described in Sanna et al. (2012); Zhang et al. (2017a); Ribeiro et al. (2017): we fitted the average power spectra with a model consisting of a constant component to represent the power produced by the Poissonian nature of the light curve, plus one or two Lorentzians to represent the kHz QPOs, and we accepted as QPOs those peaks in the averaged power spectrum of an observation where the ratio between the normalization of the Lorentzian function and its negative 1σ error was larger than 3, and the quality factor Q was larger than 2. We ended up with 580 observations with at least 1 kHz QPO detected.

Once we identified the observations with kHz QPOs, we created dynamical power spectra (Berger et al. 1996) using the non-overlapping 16 s segments in order to trace the frequency evolution of the QPOs during each observation. In the best cases we were able to trace the frequency evolution down to 16 s, whereas in the worst cases we assigned the frequency measured from the averaged PDS for each of the detected QPOs for an entire observation. Fig. 1 shows two examples of dynamical power spectra in the best and worst case scenarios. For the intermediate cases we combined as many non-overlapping 16 s segments as necessary to identify the QPO in the

Table 1. Overview of the QPO frequency intervals used to combine the different power spectra of 4U 1636–53. The uncertainties of the rms fractional amplitude and QPO frequency represent the 1σ confidence interval propagated from the best-fitting Lorentzian and the modelled background count-rate, as explained in the text.

Frequency interval (Hz)	Number of 16 s segments	Average frequency (Hz)	rms (%)
Lower kHz QPO			
470–590	1859	574.1 ± 2.6	4.39 ± 0.40
590–620	2141	611.1 ± 1.2	4.55 ± 0.32
620–670	8009	651.9 ± 0.8	6.62 ± 0.38
670–715	6302	698.3 ± 0.5	7.36 ± 0.21
715–750	6385	732.1 ± 0.4	8.08 ± 0.27
750–790	6862	765.2 ± 0.4	8.22 ± 0.32
790–820	7573	809.1 ± 0.2	7.86 ± 0.19
820–850	9569	838.7 ± 0.2	7.55 ± 0.34
850–880	10738	864.2 ± 0.1	7.15 ± 0.21
880–910	11919	894.4 ± 0.2	5.42 ± 0.19
910–975	8422	917.8 ± 0.4	3.88 ± 0.10
Upper kHz QPO			
440–540	4033	486.2 ± 6.4	13.7 ± 0.8
540–650	3872	604.4 ± 2.9	11.9 ± 0.5
650–750	6911	718.7 ± 2.2	12.4 ± 0.5
750–810	7662	780.0 ± 1.5	11.3 ± 0.4
810–870	5258	838.5 ± 1.5	10.0 ± 0.4
870–930	4669	892.3 ± 2.1	8.6 ± 0.3
930–1025	1316	947.0 ± 3.8	5.8 ± 0.4
1025–1165	382	1147.1 ± 17.1	3.0 ± 1.3
1165–1250	4087	1223.1 ± 2.8	2.3 ± 0.1

dynamical power spectra. At the end of this procedure we were able to assign at least one QPO frequency to each 16 s segment of an observation.[1] If there were two simultaneous kHz QPOs in an observation, we assigned two frequencies to each segment of that observation, corresponding to the lower and upper kHz QPOs, respectively. For observations with only 1 kHz QPO, we used the colour–colour diagram to identify the QPO as the lower or the upper kHz QPO as done by Ribeiro et al. (2017).

We divided the frequency range covered by the QPOs into 9 frequency intervals for the upper kHz QPO and 11 frequency intervals for the lower kHz QPO, as shown in Table 1. This selection is the same used by Ribeiro et al. (2017), and was chosen to achieve a compromise between having a sufficient number of observations with QPOs at each of the frequency intervals and having enough frequency intervals for a meaningful analysis. We then selected and combined all 16 s power spectra with an assigned QPO frequency in each of those intervals, separately for each QPO. Note that this is different from the technique used in Zhang et al. (2017a) and Ribeiro et al. (2017), where each observation was assigned only one averaged QPO frequency (for each kHz QPO detected), which corresponds to the approach of the worst case scenario in this work, illustrated in the bottom row of Fig. 1.

For each observation with a kHz QPO, we computed PDS at various energy bands. The chosen energy bands are shown in Table 2. This energy selection is the same one used by de Avellar et al. (2016). We took into account the slow drift in the energy-to-channel relation of the PCA detectors to define the boundaries of the energy bands in the different *RXTE*/PCA gain epochs (de Avellar et al. 2013). We then measured the rms amplitude of each QPO in the averaged PDS for each of the selected frequency intervals in the full energy band (nominally 2–60 keV), and at the selected energy bands as follows:

[1] In the worst case scenario explained above, we assigned the same frequency to all 16 s intervals of an observation.

Table 2. Overview of energy bands used to select individual power spectra. The channel boundaries of each band were adapted for each *RXTE*/PCA epoch to correspond approximately to the same energy band. The uncertainties of the rms fractional amplitude represent the 1σ confidence interval propagated from the best-fitting Lorentzian and the modelled background count-rate; as explained in the text, we measured the rms amplitude in the power spectra after shifting the lower and upper kHz QPOs, respectively, to a single frequency using the shift-and-add technique.

Average energy (keV)	Channel selection by Epoch 3rd Epoch	4th Epoch	5th Epoch	rms (%) Lower kHz QPO	Upper kHz QPO
4.2	08–12	07–10	07–11	4.3 ± 0.4	5.4 ± 0.3
6.0	13–17	11–05	12–15	6.0 ± 0.2	6.4 ± 0.5
8.0	18–23	16–21	16–21	8.2 ± 0.3	9.3 ± 0.5
10.2	24–29	22–25	22–25	9.5 ± 0.6	13.1 ± 1.3
12.7	30–41	26–35	26–35	11.0 ± 0.8	13.1 ± 1.1
16.3	42–46	36–39	36–41	9.8 ± 1.2	16.2 *
18.9	47–55	40–46	42–49	7.2 ± 1.3	19.1 *

* Upper limit at 95% confidence.

We fitted the averaged PDS in the frequency range of 200–1500 Hz in each energy band and for each QPO frequency interval with a constant, to represent the Poisson noise, and 1 or 2 Lorentzians to represent the kHz QPOs. We binned the power spectra by a factor of 50, which yielded a frequency resolution of ~3 Hz. At first we let all the parameters of the QPOs free between energy bands. When we were not able to detect a significant QPO at a specific energy band, we fixed the frequency and width of the QPO to be the same values as those in the full-energy band to calculate upper limits.

We used the integrated power of the best-fitting Lorentzian, P, to represent the total power of the QPO. We then calculated the rms amplitude in per cent units as

$$rms = \sqrt{\frac{P}{S+B}} \cdot \left(\frac{S+B}{S}\right) \cdot 100\,, \quad (1)$$

where S is the source count rate and B is the background count rate. We calculated the source count rate as the difference between the total observed count rate, C, and the background count rate.

To estimate the background count rate we used the *Ftool* `pcabackest` based on the `Standard2` light curves of each observation for each of the energy bands investigated. We measured, for each of the frequency intervals, the average and the peak-to-peak variation of the background count rate of the combined observations with QPO frequency within that interval.

Using the procedure above we obtained the rms amplitude of both kHz QPOs in each energy band and frequency interval. We used `pyxspec` version 2.0.1 (Arnaud 1996) to fit the rms-versus-energy and rms-versus-frequency relations with simple analytical models. The models fitted have no physical motivation, and some of the fits are statistically unacceptable, but they reveal the quantitative differences between the different relations.

In all the fit procedures presented in the next section we used the 1σ error to represent the uncertainties of the fitted variable. On the occasions where the fitted Lorentzian power was not significantly different from zero but still positive, we used the calculated values of the fractional rms amplitude as valid measurements during the

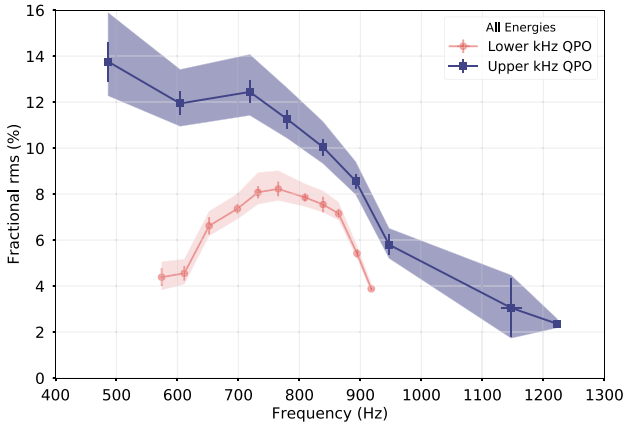

Figure 2. The marginal distribution of the rms amplitude of the kHz QPOs of 4U 1636−53 as a function of QPO frequency, averaged over the full PCA energy band. The lower kHz QPO is shown in light red and the upper kHz QPO in dark blue. The shaded areas represent the range of rms values assuming a background count rate between zero and two times larger than the maximum value given by the `pcabackest` tool, including the statistical errors in those cases. (A colour version of this figure is available in the on-line version of the paper).

fit procedures. In some cases the best-fitting Lorentzian yielded a negative integrated power at the expected QPO frequency in relation to the Poisson level; for those cases we used zero as the value of the rms amplitude and the 95 per cent confidence upper limit as the error bar for the fit routines. In both cases we plot the 95 per cent confidence upper limit to provide the correct visualization, and in the tables we give both the measurements and the upper limits.

3 RESULTS

In this section we show the results of the rms amplitude of both kHz QPOs in the 2D space of QPO frequency and photon energy. In Section 3.1 we show the rms amplitude marginalized over, respectively, QPO frequency and energy, which we call the marginal distributions of the rms amplitude. In Section 3.2 we show the results of, respectively, the rms amplitude versus QPO frequency given the photon energy and rms amplitude versus energy given the QPO frequency, which we call the conditional distributions of the rms amplitude. Finally, in Section 3.3 we show the joint distribution of the rms amplitude versus QPO frequency and photon energy.

3.1 The marginal distributions of rms amplitude versus QPO frequency and photon energy

In Fig. 2 we show the marginal distribution of the rms amplitude of the lower and upper kHz QPO in 4U 1636−53 in the full energy band of the PCA detectors, nominally 2–60 keV, as a function of frequency. We used the shift-and-add technique (Méndez et al. 1998a) to average the power spectra with different QPO frequencies and obtain the marginal distribution of rms amplitude as a function of photon energy (see below). For the conditional distributions (Section 3.2) of the rms fractional amplitude as a function of frequency and energy, we did not use the shift-and-add technique since the frequency of the QPO does not change much within the chosen frequency intervals and the averaged PDS can be fitted directly with a Lorentzian in order to obtain the QPO rms amplitude.

It is apparent from Fig. 2 that in 4U 1636−53 the relation between amplitude and frequency of the lower kHz QPO is different than that of the upper kHz QPO. The rms amplitude of the lower kHz QPO increases with frequency from ∼4 per cent at 570 Hz up to ∼8 per cent at 750 Hz, where it peaks, and then decreases back to ∼4 per cent as the frequency increases up to ∼920 Hz. On the contrary, the rms amplitude of the upper kHz QPO decreases from ∼14 per cent down to ∼2 per cent as the QPO frequency increases from 480 to 1200 Hz (Di Salvo et al. 2001; Mendez et al. 2001; Barret, Olive & Miller 2005; Mendez 2006): As previously noted by Ribeiro et al. (2017), besides the overall decreasing trend, the rms amplitude of the upper kHz QPO shows a hump at around ∼700 Hz.

To check the effect of the modelling of the background upon our results, we estimated the change of the fractional rms amplitude if the averaged background count rate, B, was either 0 or a factor of 2 times larger than the maximum value obtained using `pcabackest` as described in Section 2. We show the result of this test by the shaded area in Fig. 2. We chose a factor of 2 to demonstrate the robustness of the rms values. As can be seen from the figure, the trends are not significantly affected by this exaggerated uncertainty on the background count rate (See also de Avellar et al. 2016).

We fitted the relations in Fig. 2 with simple analytical functions, as done by Ribeiro et al. (2017). For the lower kHz QPO we fitted a Gaussian function defined as

$$f(\nu) = N \cdot e^{-\frac{(\nu-\nu_0)^2}{2\sigma^2}}\,, \tag{2}$$

where ν is the QPO frequency, ν_0 is the centroid, N is the height, and σ is the standard deviation of the Gaussian. The best fit yielded $\nu_0 = 761 \pm 2$ Hz, $\sigma = 134 \pm 3$ Hz, and $N = 8.6 \pm 0.1$ per cent.

For the upper kHz QPO we fitted a model consisting of a linear function plus a Gaussian. The linear function was defined as

$$f(\nu) = -s_1 \cdot (\nu - \nu_i)\,, \tag{3}$$

where ν_i is the frequency at which the rms is zero, s_1 is the slope of the function, and ν is the QPO frequency. The best fit yielded a slope $s_1 = 0.014 \pm 0.01$ per cent/Hz, an intercept $\nu_i = 1381 \pm 16$ Hz, and a Gaussian centred at $\nu_0 = 765 \pm 17$ Hz with $\sigma = 103 \pm 21$ Hz and $N = 2.6 \pm 0.5$ per cent. These results are consistent with the ones presented by Ribeiro et al. (2017), with the small differences due to the fact that we are averaging power spectra taken every 16 s, whereas in Ribeiro et al. (2017) we averaged the power spectra for each observation before separating them into frequency intervals.

In Fig. 3 we show the marginal distribution of the rms amplitude of the kHz QPOs as a function of energy. To fit the QPO in each band we used the shift-and-add technique (Méndez et al. 1998a) to shift the QPOs of all the observations to a common frequency. We applied this shift separately for the lower and upper kHz QPOs. The rms amplitude of the upper kHz QPO increases from ∼5 per cent to ∼17 per cent as the energy increases from 4 to 19 keV. (The two last measurements are upper limits of the rms amplitude.) As shown by the shaded area, at energies above 13 keV the measurements are affected by the uncertainties in the background count rate. On the other hand, the rms amplitude of the lower kHz QPO increases at first from ∼5 per cent to ∼11 per cent as the energy increases from 4 to ∼12 keV, and then decreases to ∼7 per cent as the energy increases from ∼12 to 19 keV. As we can see from the shaded area limits, if we allow the background count rate to vary from 0 to a factor of 2 higher than the maximum value estimated using `pcabackest`, the effect of this systematic error on the rms values

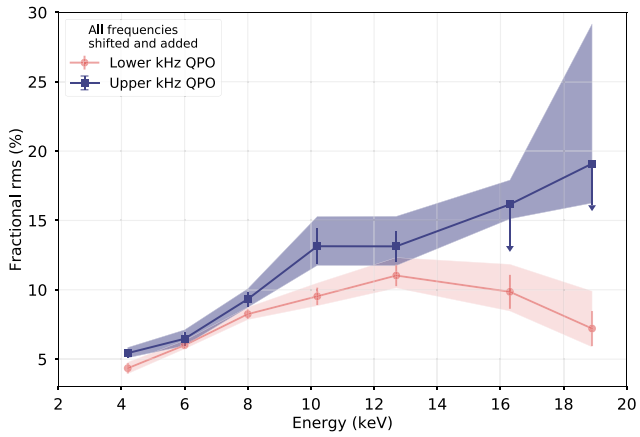

Figure 3. The marginal distribution of the rms amplitude of the kHz QPOs of 4U 1636−53 as a function of photon energy, averaged overall detected QPO frequencies using the shift-and-add technique (Méndez et al. 1998a) separately for the lower and upper kHz QPOs. The lower kHz QPO is shown in light red and the upper kHz QPO in dark blue. The shaded areas represent the range of rms values assuming a background count rate between zero and two times larger than the maximum value given by the `pcabackest` tool, including the statistical errors in those cases. When an upper limit is present the lower end of shaded area is also an upper limit. (A colour version of this figure is available in the on-line version of the paper).

does not change the observed shape of the rms as a function of energy.

We proceeded to quantify the shape of the marginal distribution of the rms amplitude versus energy in the same manner as for the marginal distribution of rms amplitude versus frequency, above. We first fit the rms-versus-energy relation of the lower kHz QPO with a linear function of the type $rms(E) = s_1 \times E$, which results in a linear slope of $s_1 = 0.88 \pm 0.02$ per cent keV^{-1} with a reduced chi-squared value $\chi^2_\nu = 15.2$ for 6 degrees of freedom. We then fit the same rms-versus-energy relation with a broken-line function defined as

$$rms(E) = \begin{cases} s_1 \cdot E, & \text{if } E \leq E_{\rm break} \\ s_2 \cdot E + (s_1 - s_2) \cdot E_{\rm break}, & \text{if } E \geq E_{\rm break} \end{cases} \quad (4)$$

where $E_{\rm break}$ is the break energy, and s_1 and s_2 are the slopes before and after the break, respectively. The fit yielded a reduced chi-squared of $\chi^2_\nu = 0.55$ for 4 degrees of freedom. Compared to the fit with a linear function, the F-test probability is $6 \cdot 10^{-4}$. The broken line model yielded a slope before the break $s_1 = 0.99 \pm 0.02$ per cent keV^{-1}, slope after the break $s_2 = -0.6 \pm 0.2$ per cent keV^{-1}, and a break energy $E_{\rm break} = 11.8 \pm 0.3$ keV. Compared to a fit with the slope after the break fixed to zero the F-test probability is 2.8×10^{-2}.

For the upper kHz QPO a linear function with slope $s = 1.15 \pm 0.04$ per cent keV^{-1} yielded a reduced chi-squared $\chi^2_\nu = 1.89$ for 6 degrees of freedom. A broken line model yields a reduced chi-squared $\chi^2_\nu = 1.33$ for 4 degrees of freedom, with $s_1 = 1.18 \pm 0.04$ per cent keV^{-1}, $s_2 = 2.7 \pm 2.7$ per cent keV^{-1}, and $E_{\rm break} = 12.4 \pm 1.5$ keV. The F-test between the linear and a broken-line model yields a probability of 0.22. Since the slope after the break was not significantly different from zero, we fixed $s_2 = 0$, which yielded a reduced chi-square $\chi^2_\nu = 1.27$ for 5 degrees of freedom, the slope before the break is $s_1 = 1.18 \pm 0.04$ per cent keV^{-1}, and the break energy $E_{\rm break} = 10.9 \pm 0.9$ keV. An F-test between the broken line models with s_2 free to vary and with s_2 fixed to zero yields a probability of 0.43.

3.2 The conditional distributions of the rms amplitude versus QPO frequency and energy

In this section we study the relation between rms amplitude and frequency of the QPOs in different energy bands, and of the rms amplitude of the QPOs and energy at different QPO frequencies, which we call conditional distributions. Initially, we looked at observations that contained a QPO detectable in most energy bands and confirmed that the frequency of the kHz QPO in different bands is consistent with being the same, within the chosen frequency intervals, during the same observation. This is an important

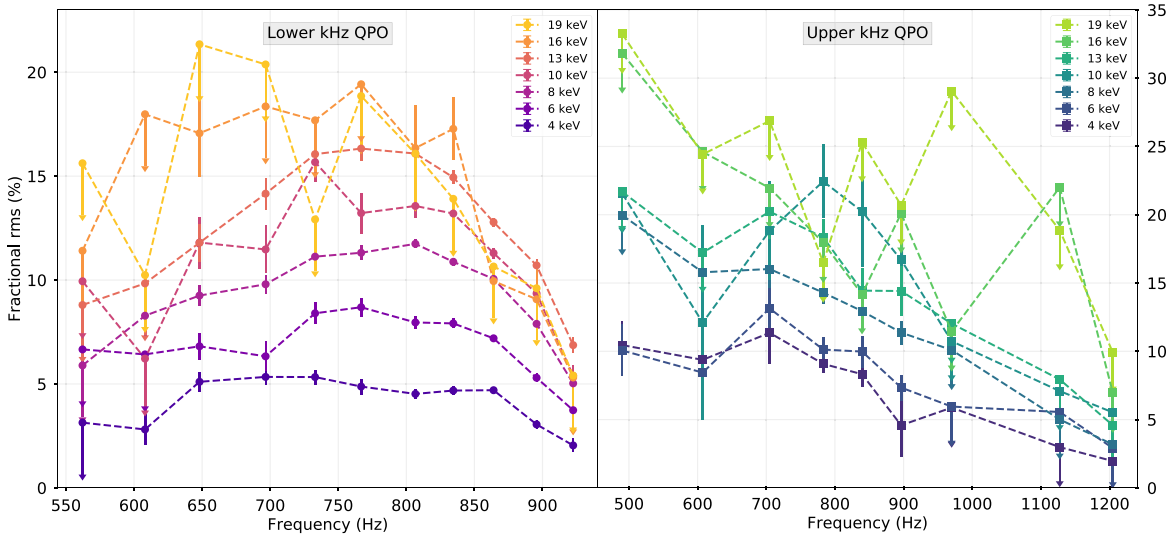

Figure 4. The conditional distribution of the rms amplitude of the lower and upper kHz QPOs, left-hand and right-hand panels, respectively, of 4U 1636−53 as a function of QPO frequency for a given energy. Each energy band is represented by a different colour. (A colour version of this figure is available in the on-line version of the paper).

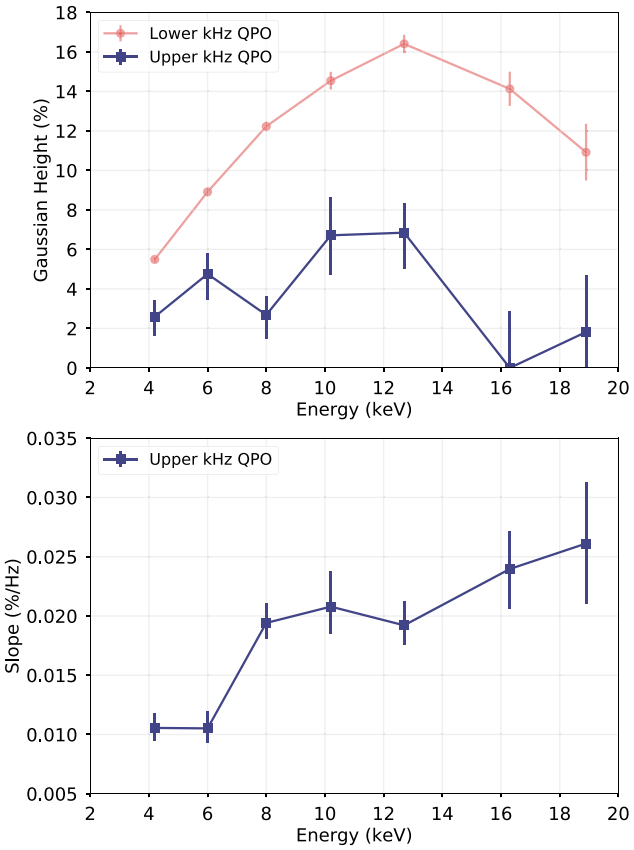

Figure 5. Upper panel: The normalization of the Gaussian from the best-fitting model to the rms amplitude of the lower kHz QPO (light red circles) and the upper kHz QPO (dark blue squares) of 4U 1636−53 plotted in Fig. 4. Lower panel: The slope of the best-fitting model to the rms amplitude of the upper kHz QPO of 4U 1636−53 plotted in Fig. 4 (a coloured version of this figure is available in the on-line version of the paper).

information to investigate the nature of kHz QPOs (Mukherjee & Bhattacharyya 2012; Wang 2016).

In Fig. 4 we show the conditional distribution of the rms amplitude as a function of QPO frequency for both kHz QPOs in different energy bands. It is apparent from Fig. 4 that the shape of the rms amplitude with frequency remains roughly the same as in Fig. 2 for both kHz QPOs, but the overall amplitude increases as the energy increases from 4 to 19 keV. As in Section 3.1, we fit the conditional rms-versus-frequency relation at different energies with analytical functions. For the lower kHz QPO we fit a Gaussian function (equation 2). The centroid and the width of the Gaussian are consistent with being the same for all energy bands, so we fitted all these curves simultaneously with these parameters tied during the fit, whereas the normalization of the Gaussian was left free to vary. The best fit yields a centroid $\nu_0 = 761 \pm 3$ Hz and a width $\sigma = 130 \pm 3$ Hz, with a a reduced chi-squared $\chi^2_\nu = 1.8$ for 68 degrees of freedom. We plot the normalization of the Gaussian as a function of energy in the upper panel of Fig. 5 as red data points.

A look at the right-hand panel of Fig. 4 suggests that the slope of the rms amplitude of the upper kHz QPO becomes steeper as photon energy increases, and that the hump in the rms versus frequency at ∼800 Hz in Fig. 2 (see also Ribeiro et al. 2017) is present, and at roughly the same frequency, in all energy bands, the exception being the highest energy band for which we only have upper limits for the rms amplitude. To quantify this, we fitted all the curves simultaneously with a model consisting of a linear function that decreases with energy parametrized as in equation (3). We also added a Gaussian function (equation 2) to the model to fit the hump. We kept the intercept point, ν_i, tied during the fit, since when we let it free to vary between energy bands the best-fitting values are consistent with being the same for all the energy bands. The Gaussian parameters, with exception of the normalization, N, were tied together between all energy bands since, when we left these parameters free the best-fitting values were consistent with being the same. The best fit yields $\nu_i = 1398 \pm 24$ Hz. For the Gaussian component we obtain $\nu_0 = 771 \pm 16$ Hz and $\sigma = 93 \pm 21$ Hz. This fit yielded a reduced chi-square $\chi^2_\nu = 0.6$ for 46 degrees of freedom. We show the slope of the linear function as a function of energy in the lower panel of Fig. 5 and the normalization of the hump as dark blue data points in the upper panel of the same figure.

We also fitted the data on both panels of Fig. 4 simultaneously and tied the parameters ν_0 and σ of the Gaussian function that describes the shape of the relation for the lower kHz QPO and the same parameters of the Gaussian function associated with the *hump* in the relation for the upper kHz QPO. The fit yielded a chi-square $\chi^2 = 153.80$ for 116 degrees of freedom. The best-fitting parameter for the Gaussian function were $\nu_0 = 761 \pm 3$ Hz and $\sigma = 129 \pm 4$ Hz, and, the other parameters were consistent with the ones presented above, including the normalizations of the Gaussian shown in Fig. 5. Fitting the data from the lower and upper kHz QPO separately as described in the last two paragraphs yielded a combined chi-square of $\chi^2 = 151.4$ for 114 degrees of freedom. These values yield an F-test probability of ∼0.4, meaning that there is no statistical benefit in keeping the Gaussian parameters of the lower kHz QPO and the hump of the upper kHz QPO free. In other words, our results indicate that the parameters of the Gaussian that fits the rms–frequency relation of the lower kHz QPO, are consistent with those of the Gaussian that fits the *hump* in the rms–frequency relation of the upper kHz QPO.

In Fig. 6 we show, separately for each QPO, the conditional distributions of the rms amplitude as a function of energy for each QPO frequency interval. The rms amplitude of both QPOs increases with energy as energy increases from ∼4 to ∼14 keV: above 14 keV the data presents several upper limits and the trend is no longer clear. The slope of the rms versus energy relation of the lower kHz QPO (left-hand panel of Fig. 6) appears to increase at first and then decrease as the frequency of the QPO increases further. On the other hand, the slope of the rms versus energy relation of the upper kHz QPO decreases as the frequency of the QPO increases.

To quantify this, we fitted the conditional distributions in Fig. 6 with a broken line model (equation 4) for both kHz QPOs. At first we let all other parameters free to vary during the fit, but we noticed that the break energy and the slope after the break were consistent with being the same, for each QPO separately in all QPO frequency intervals. We therefore tied the energy break and the slope above the break to be the same in all QPO frequency intervals and allowed only the slope before the break to vary for the different frequency intervals. For the lower kHz QPO the best fit yields an energy break $E_{\rm break} = 12.0 \pm 0.2$ keV and a slope after the break $s_2 = -0.5 \pm 0.1$ per cent keV^{-1}, the reduced chi-squared is $\chi^2_\nu = 1.4$ for 64 degrees of freedom. We show the slope before the break, s_1, as a function of QPO frequency as light red data points in Fig. 7.

For the upper kHz QPO the slope after the break is consistent with being zero in all QPO frequency intervals, so we fixed $s_2 = 0$. The best fit to the upper kHz QPO yields an energy break $E_{\rm break} = 9.3 \pm 0.7$ keV and a reduced chi-squared $\chi^2_\nu = 0.7$ for 52 degrees

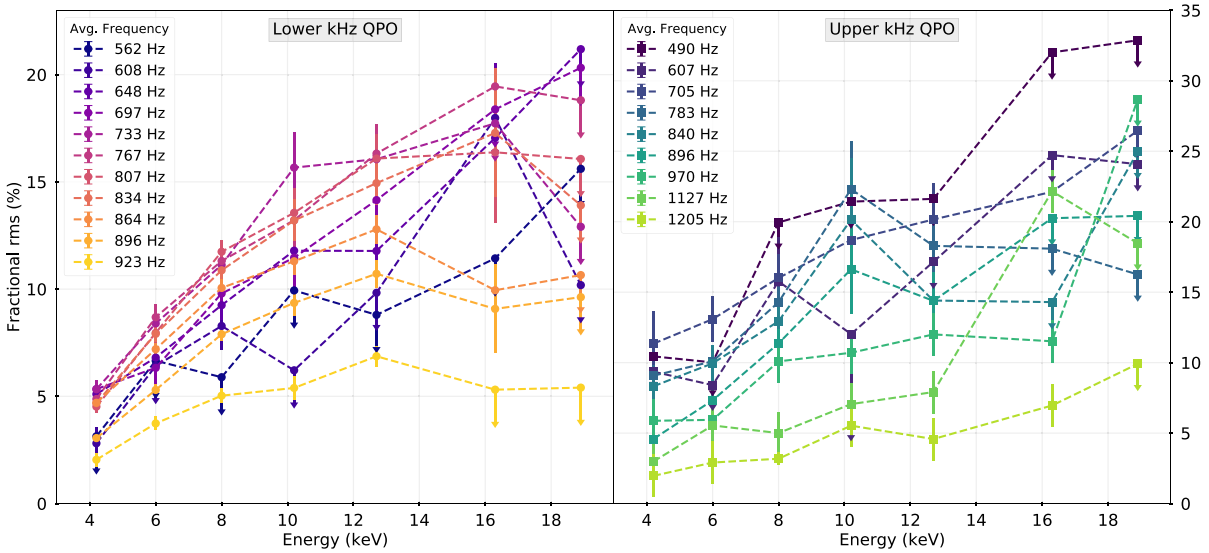

Figure 6. The conditional distribution of the rms amplitude of the lower and upper kHz QPO, left-hand and right-hand panels, respectively, of 4U 1636−53 as a function of photon energy for given QPO frequency. (A colour version of this figure is available in the on-line version of the paper).

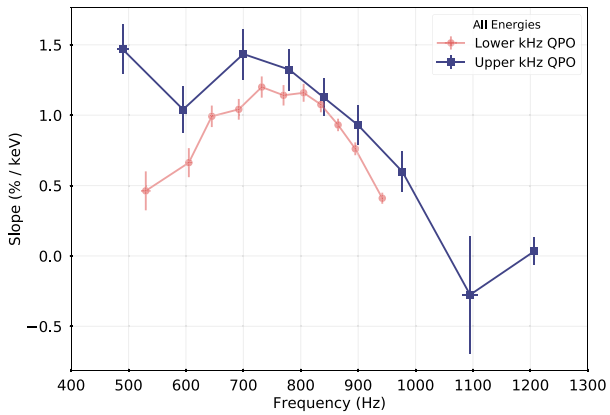

Figure 7. The slope before the break of the conditional distribution of the rms amplitude as a function of energy for given frequency intervals (Fig. 6), for both kHz QPOs. The lower kHz QPO is shown as light red circles and the upper kHz QPO is shown as dark blue squares. (A colour version of this figure is available in the on-line version of the paper).

of freedom; we show the slope before the break as a function of QPO frequency as dark blue data points in Fig. 7.

The normalization of the Gaussian fitted to the curve of the rms amplitude versus frequency for the lower kHz QPO (Fig. 4, left-hand panel) reproduces the shape of the rms amplitude versus energy for that same QPO (Fig. 5), whereas for the upper kHz QPO the relation is not as straightforward. The bottom panel of Fig. 5 shows the slope of the linear function fitted to the rms amplitude versus frequency relations for the upper kHz. The slopes increase with energy, but this increase cannot be translated into a fractional rms amplitude to allow a direct comparison with the upper panel of Fig. 5. It is interesting to notice that the normalization of the 'hump' in the rms-versus-frequency relation of the upper kHz QPO rms, displays a similar trend to that of the normalization of the rms-versus-frequency relation of the lower kHz QPO, albeit with smaller amplitudes and larger uncertainties.

In Fig. 6 we show the relation between the fractional rms amplitude and photon energy for both kHz QPOs at different QPO frequencies. The individual relations follow the average behaviour displayed in Fig. 3. We find that the slope with which the rms increases with photon energy varies with QPO frequency. The change of slope is reflected as the general trend displayed by the rms amplitude versus frequency relation in Fig. 2. It is unclear if one is caused by the other, but it is clear that there is a relation between the rms changes with frequency and the slope with which the rms changes with energy, for both kHz QPOs.

3.3 The joint distribution of the kHz QPOs rms amplitude in the frequency-energy space

Using the conditional distributions from Figs 4 and 6, in Figs 8 and 9 we plot the rms amplitude of the kHz QPOs as a colour map in the 2D grid of QPO frequency and energy. We provide the measured values in Table 3. To improve the visualization we smoothed the data using a 2D Gaussian kernel. To represent the upper limits in these 2D plots, we used instead the rms values given by the best-fitting models, described in the previous sub-section, to represent the expected values.

We show the rms amplitude in the frequency-and-energy space for the lower kHz QPO in Fig. 8; the top panel shows the marginal distribution of the rms amplitude as a function of energy averaged over frequency, and the right-hand panel shows the marginal distribution of the rms amplitude as a function of frequency averaged over energy. As expected, the marginal distributions are a smoothed version of the plots in Figs 2 and 3. We overplot contour lines to help visualize the structure of the distribution. We show the same results for the upper kHz QPO in Fig. 9.

We see in Fig. 8 that the rms of the lower kHz QPO is almost symmetric in the frequency axis, consistent with the fact that the marginal and conditionals distribution of the rms amplitude versus QPO frequency can be fitted with a Gaussian function. As a function of energy we can see that the rms amplitude of the lower kHz QPO increases and then decreases with energy.

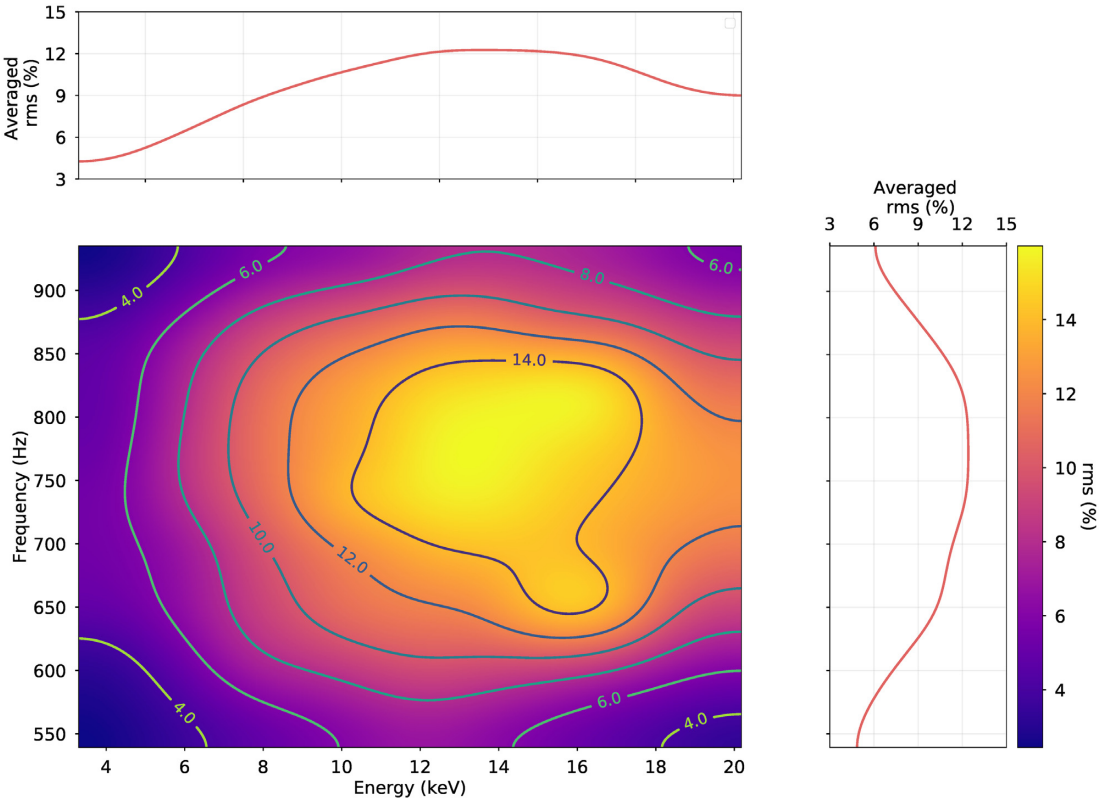

Figure 8. The joint distribution of the rms amplitude of the lower kHz QPO of 4U 1636−53 as a function of photon energy and QPO frequency. The colour scale represents the rms amplitude as indicated in the colour bar at the far right of the figure. The top and right-hand panels show the marginal distributions averaged over, respectively, QPO frequency and energy. Contour lines are shown on top of the colour map to aid visualization. (A colour version of this figure is available in the on-line version of the paper).

The topology of the rms amplitude of the upper kHz QPO shows a more complex structure, in part probably due to the fact that for several energy bands and frequency intervals we only have upper limits to the rms amplitude. We can see in Fig. 9, however, that the rms amplitude increases as photon energy increases, while it simultaneously decreases as the QPO frequency increases.

4 DISCUSSION

We present the first study of the distribution of the fractional rms amplitude of the kHz QPOs in a NS-LMXB both as a function of photon energy and QPO frequency. Previous studies of the kHz QPO had examined the dependence of the rms amplitude upon either energy or frequency, marginalizing the dependence of the rms amplitude upon the other quantity. We find that in 4U 1636−53 the change of the rms amplitude of both kHz QPOs with QPO frequency depends on energy, and is in fact connected to changes of the slope in the rms energy spectrum (rms amplitude versus energy) of the QPO. In the case of the lower kHz QPO the slope in the rms energy spectrum increases as the QPO frequency increases from ∼500 to ∼750 Hz, and then decreases when the QPO frequency increases further from ∼750 to ∼950 Hz. In parallel with that the 2−60 keV rms amplitude of the lower kHz QPO follows the same behaviour with QPO frequency. In the case of the upper kHz QPO the slope in the rms spectrum generally decreases as the QPO frequency increases from ∼500 up to ∼1200 Hz, showing a local hump at around 700 Hz. Also in this case, the frequency dependence of the 2−60 keV rms amplitude of the upper kHz QPO mirrors this behaviour. Finally, we find that the kHz QPO frequency is the same at different energy bands, and that the rms amplitude of the lower kHz QPO in 4U 1636−53 drops significantly at energies above 12 keV, compared to the extrapolation of the rms–energy relation below that energy.

4.1 The drop of the rms amplitude of the lower kHz QPO at high energies

The shape of the rms energy spectrum is essential to understand the origin of kHz QPOs, since it provides a link between a timing property (amplitude of the QPO) and a spectral property (high-energy emission) of the source. Above 10 keV, where the kHz QPOs have an rms amplitude of ∼10 per cent or more (Figs 3 and 6; see also Berger et al. 1996; Mendez et al. 2001; Gilfanov et al. 2003; Peille et al. 2015; Troyer et al. 2018) the accretion disc contribution to the energy spectrum of LMXBs is negligible, and the spectrum is dominated by the Comptonizing component. We find that the rms amplitude of the lower kHz QPO declines significantly at photon energies above ∼12 keV, implying that the efficiency of the radiative mechanism responsible for this QPO decreases as the energy increases above that energy.

Mukherjee & Bhattacharyya (2012) reported that the rms fractional amplitude of the lower kHz QPO in 4U 1728−34 drops at high energies. However, the result reported by Mukherjee & Bhattacharyya (2012) is based on an upper limit measurement

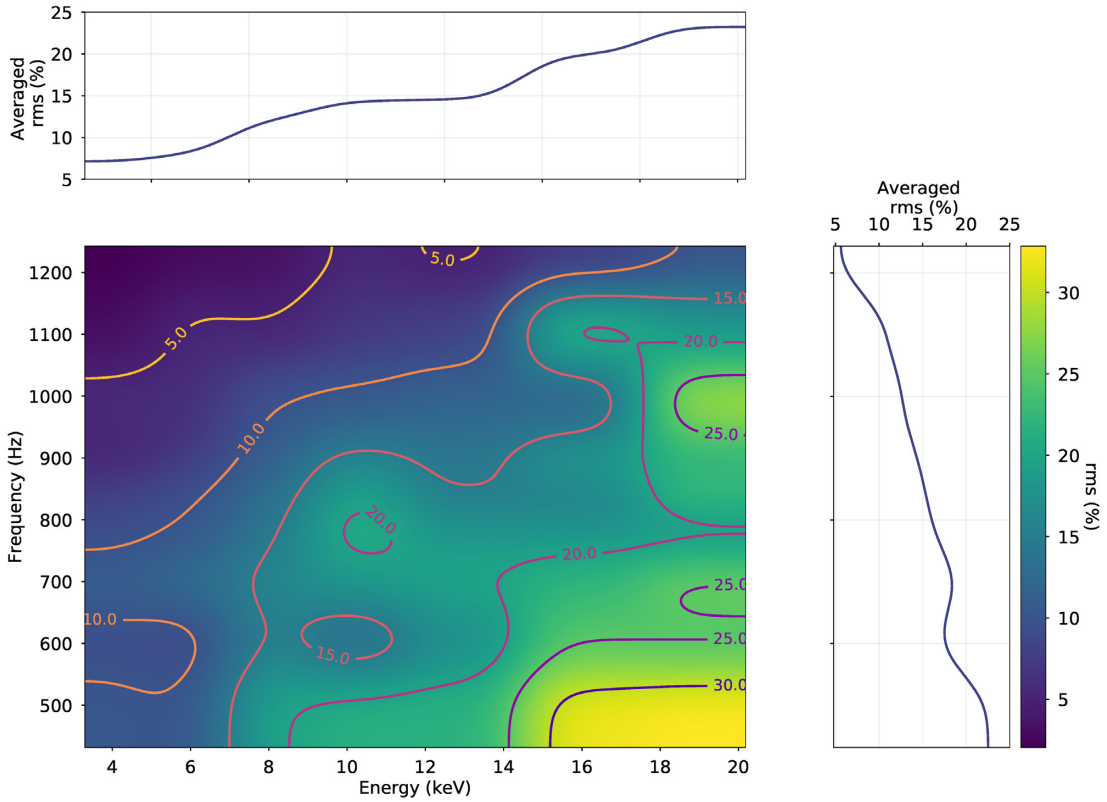

Figure 9. Same as Fig. 8 for the upper kHz QPO of 4U 1636−53. (A colour version of this figure is available in the on-line version of the paper).

Table 3. The fractional rms amplitude of the kHz QPOs in 4U 1636−53 as a function of the energy band and the QPO frequency interval. Uncertainties are the propagated 1σ error from the best fit to each power spectrum.

Frequency interval (Hz)	Energy band (keV) 3.0–5.0	5.0–7.0	7.0–9.0	9.0–11.0	11.0–15.0	15.0–17.0	17.0–20.0
Lower kHz QPO							
470–590	2.0 ± 1.4 (3.1 *)	5.0 ± 1.2 (6.7 *)	4.1 ± 1.4 (5.9 *)	6.6 ± 2.6 (9.9 *)	5.9 ± 2.2 (8.8 *)	0.0 ± 10.2 (11.4 *)	0.0 ± 13.0 (15.6 *)
590–620	2.8 ± 0.7	5.0 ± 0.9 (6.4 *)	8.3 ± 1.1	0.0 ± 5.2 (6.2 *)	7.9 ± 1.4 (9.8 *)	13.6 ± 3.8 (18.0 *)	0.0 ± 11.8 (10.2 *)
620–670	5.1 ± 0.5	6.8 ± 0.7	9.3 ± 0.7	11.8 ± 1.6	11.8 ± 1.3	17.1 ± 3.5	16.5 ± 5.0 (21.2 *)
670–715	5.3 ± 0.4	6.3 ± 0.8	9.8 ± 0.6	11.5 ± 1.5	14.2 ± 1.3	14.5 ± 3.3 (18.4 *)	14.8 ± 5.2 (20.3 *)
715–750	5.3 ± 0.4	8.4 ± 0.7	11.1 ± 0.7	15.7 ± 1.7	16.1 ± 1.4	14.7 ± 3.5 (17.7 *)	0.0 ± 10.9 (12.9 *)
750–790	4.9 ± 0.4	8.7 ± 0.6	11.3 ± 0.6	13.2 ± 1.5	16.3 ± 1.4	14.8 ± 3.6 (19.5 *)	12.3 ± 5.7 (18.8 *)
790–820	4.5 ± 0.3	8.0 ± 0.5	11.7 ± 0.5	13.6 ± 1.1	16.1 ± 1.2	16.7 ± 3.5	12.2 ± 4.0 (16.1 *)
820–850	4.7 ± 0.2	7.9 ± 0.4	10.9 ± 0.5	13.2 ± 1.0	14.9 ± 1.0	16.8 ± 2.9	10.8 ± 3.5 (13.9 *)
850–880	4.7 ± 0.2	7.2 ± 0.3	10.1 ± 0.4	11.3 ± 0.6	12.8 ± 0.7	9.7 ± 0.9	0.0 ± 19.0 (10.7 *)
880–910	3.1 ± 0.2	5.3 ± 0.3	7.9 ± 0.3	9.4 ± 0.6	10.7 ± 0.6	10.3 ± 2.2	6.7 ± 2.0 (9.6 *)
910–975	2.0 ± 0.3	3.7 ± 0.3	5.0 ± 0.3	5.4 ± 0.5	6.9 ± 0.5	3.5 ± 1.1 (5.3 *)	3.0 ± 1.1 (5.4 *)
Upper kHz QPO							
440–540	10.4 ± 1.8	10.0 ± 2.0	18.0 ± 1.6 (19.9 *)	16.2 ± 4.0 (21.4 *)	18.5 ± 2.5 (21.6 *)	25.2 ± 5.8 (32.0 *)	23.5 ± 7.9 (32.9 *)
540–650	9.4 ± 1.2	8.4 ± 1.4	15.8 ± 3.1	12.0 ± 7.2	14.8 ± 1.9 (17.2 *)	19.2 ± 4.7 (24.7 *)	15.6 ± 7.1 (21.1 *)
650–750	11.3 ± 2.3	13.1 ± 1.6	16.0 ± 1.7	18.7 ± 4.0	20.2 ± 2.6	15.0 ± 5.6 (22.1 *)	18.0 ± 7.3 (26.5 *)
750–810	9.1 ± 0.7	10.1 ± 1.1	14.3 ± 1.1	22.3 ± 3.4	18.3 ± 1.9	12.2 ± 4.8 (18.1 *)	1.7 ± 45.1 (16.3 *)
810–870	8.3 ± 0.9	10.0 ± 1.3	12.9 ± 1.1	15.2 ± 1.9	15.3 ± 1.5	4.0 ± 14.2 (14.3 *)	18.5 ± 6.0 (25.0 *)
870–930	4.6 ± 2.3	7.3 ± 1.0	11.4 ± 1.0	16.6 ± 3.2	14.4 ± 2.1	14.9 ± 4.4 (20.2 *)	10.7 ± 8.9 (20.4 *)
930–1025	4.5 ± 0.9 (5.9 *)	3.1 ± 2.6 (5.9 *)	8.8 ± 0.8 (10.1 *)	6.7 ± 3.2 (10.7 *)	9.5 ± 1.8 (12.0 *)	0.0 ± 11.6 (11.5 *)	21.1 ± 6.5 (28.7 *
1025–1165	0.0 ± 3.2 (3.0 *)	0.0 ± 4.7 (5.5 *)	0.0 ± 4.6 (5.0 *)	0.0 ± 8.0 (7.1 *)	0.0 ± 7.2 (7.9 *)	8.8 ± 14.3 (22.2 *)	0.0 ± 21.5 (18.5 *)
1165–1250	1.3 ± 0.5 (2.0 *)	2.2 ± 0.5 (2.9 *)	3.2 ± 0.5	4.5 ± 0.7 (5.5 *)	3.4 ± 0.8 (4.6 *)	2.2 ± 6.0 (7.0 *)	5.3 ± 4.1 (9.9 *)

* Upper limit at 95% confidence.

of the fractional rms amplitude of the kHz QPO in this source at a high-energy band (approximately 10–20 keV), which was calculated in such a manner that underestimates the real QPO amplitude. Mukherjee & Bhattacharyya (2012) calculated their upper limit from the power measured in a single frequency bin of width ∼3 Hz of the power spectrum at the expected QPO frequency; this calculation ignores the width of the QPO, which was around 10 Hz when the QPO was significantly detected in the

power spectrum (Mukherjee & Bhattacharyya 2012). Considering the width of the QPO, the correct 95 per cent confidence upper limit would be ∼8 per cent. This revised upper limit is consistent with the results of Peille et al. (2015) and Troyer et al. (2018), who find that the rms amplitude of the lower kHz QPO in 4U 1728−34 in the 10–20 keV energy band is ∼8–9 per cent

While our results for 4U 1636−53 agree with their claim that in 4U 1728−34 the fractional rms amplitude of the lower kHz QPO drops at high energies, the drop is not as abrupt as the one reported by Mukherjee & Bhattacharyya (2012) for 4U 1728−34 on the basis of an underestimated upper limit.

4.2 The radiative mechanism(s) behind the kHz QPOs

The plot of the rms amplitude of the upper kHz QPO as a function of frequency for the full energy band displays a local maximum at ∼765 Hz that we call a 'hump'. As discussed by Ribeiro et al. (2017), it is curious that this 'hump' happens at a frequency with the maximum in the relation between the rms amplitude and the frequency of the lower kHz QPO. From our fits we cannot discard that the hump is present in all energy bands investigated (see Fig. 4). Our results are consistent with the scenario proposed by Ribeiro et al. (2017; see also Mendez 2006; Sanna et al. 2010; de Avellar et al. 2013) that there is a radiative mechanism that is more efficient at ∼750 Hz and influences the rms amplitude of both kHz QPO, whereas there is another mechanism that acts only upon the upper kHz QPO and drives the more or less linear decay of the rms amplitude of this QPO with frequency.

Lee et al. (2001; see also also de Avellar et al. 2013; Ribeiro et al. 2017; Zhang et al. 2017a) suggested that this mechanism that acts both upon the lower and the upper kHz QPO is a resonance between the source of soft photons (the neutron-star or the accretion disc) and the Comptonizing medium. The quality factor of the lower kHz QPO peaks at around the same frequency (Belloni, Méndez & Homan 2005; Barret et al. 2006), and this is also the frequency interval that shows the largest phase lags and the highest coherence between low- and high-energy signals of the lower kHz QPO (de Avellar et al. 2013, 2016).

As shown on Fig. 3, the fractional rms amplitude of the upper kHz QPO increases with photon energy. A fit with a broken-line model indicates that the rms amplitude either remains constant or continues increasing as energy increases; given the limitations of the *RXTE*/PCA instrument we cannot strongly argue for one or the other scenario. It is interesting to notice that the rms energy spectrum of high-frequency QPOs in black hole LMXBs (e.g. GRS 1915+105, Belloni & Altamirano 2013) shows a similar trend to the marginal distribution of rms versus energy of the upper kHz QPO in 4U 1636−53; a deeper look into how this behaviour changes with QPO frequency could shed light on the connection between the variability of neutron-star and black hole LMXBs.

4.3 Implications of the conditional distributions of rms amplitude of the kHz QPO

By analysing the relation between fractional rms amplitude with frequency, we show (Fig. 4) that this relation of the lower kHz QPO maintains its shape in different energy bands, and only its normalization changes. The slope of the relation of the rms amplitude of the upper kHz QPO with frequency, however, shows an increase and not just an achromatic shift.

As shown in Fig. 7 the slope of the lower kHz QPO rms spectrum first increases and then decreases with frequency, while, at the same time, the temperature of the accretion disc only increases (Sanna et al. 2013; Lyu, Méndez & Altamirano 2014), suggesting that the slope of the relation between the rms fractional amplitude and energy for the lower kHz QPO is not driven by the soft emission from the disc. The slope in the rms versus energy relation (Fig. 6) changes with QPO frequency in a similar fashion as the rms changes with QPO frequency, and shows a seemingly preferable frequency around ∼750 Hz for both the upper and lower kHz QPO. This reinforces the idea of a common mechanism between the two QPOs, but with an extra component for the upper kHz QPO as mentioned on Section 4.2.

The dependence of the fractional rms amplitude of the kHz QPOs upon energy presented here can be compared to that of the type-C QPOs at ∼0.15–12 Hz in black holes LMXBs presented by Zhang et al. (2017b) and Huang et al. (2018). Here we find that the rms amplitude versus energy relation increases and then decreases with energy for the lower kHz QPO, while the rms amplitude only increases with energy for the upper kHz QPO and the slope of the rms amplitude versus energy relation for the upper kHz QPO decreases as the QPO frequency increases. Both Zhang et al. (2017b) and Huang et al. (2018) find that the slope of the rms versus energy relation for the type-C QPO in, respectively, GX 339−4 and MAXI J1535−571 increases with QPO frequency.

For the upper kHz QPO, the best-fitting parameters for the relation in Fig. 4 yield $\nu_i = 1398 \pm 24$ Hz as the frequency at which the rms amplitude goes to zero, and, as mentioned in Section 3.2, this value is consistent with being the same across the different energy bands. The fact that the rms of the upper kHz QPO goes to zero at a specific frequency could reflect the dynamical mechanism that produces the QPO, e.g. if the inner radius of the accretion disc reaches the innermost stable circular orbit when the upper kHz QPO reaches that frequency.

In the sonic-point model proposed by Miller et al. (1998), this maximum QPO frequency can be used to get an upper limit of the mass of the neutron-star (Kluzniak, Michelson & Wagoner 1990; van Doesburgh, van der Klis & Morsink 2018):

$$M_{NS} \leq 2.2 \cdot \left(1000/\nu_{\rm QPO}^{\rm max}\right) \cdot (1 + 0.75\,j) \cdot {\rm M}_{\odot}\,, \quad (5)$$

where j is the angular momentum of the neutron-star, which depends on the choice of equation of state (see Morsink & Stella 1999). For the minimum and maximum values of j, given by Morsink & Stella (1999), and for $\nu_{\rm QPO}^{\rm max} = \nu_i$, we get upper limits for the mass of the neutron-star in 4U 1636−53 $M_{NS} \leq 1.77\,{\rm M}_{\odot}$ for $j = 0.17$ and $M_{NS} \leq 2.19\,{\rm M}_{\odot}$ for $j = 0.52$. As pointed out by van Doesburgh et al. (2018), equation (5) does not take into account the oblateness and internal structure of the NS on its rotation rate for fast spinning stars such as 4U 1636−53 and numerical methods are necessary to obtain accurate limits on mass and radius in these cases. The limits given above here are likely underestimated. It is outside of the scope of this paper to discuss the different equations of state or the neutron star oblateness and their implications.

4.4 The break energy

The rms amplitude as a function of energy of both the lower and upper kHz QPO display a break at around $E_b \approx 12$ keV. This connection between the kHz QPOs and the high-energy photons is an important clue to the origin of these oscillations. The maximum fitted temperature to the Comptonizing medium (kT_e) in the energy spectrum of 4U 1636−53 is also around ∼12 keV (Ribeiro et al. 2017), but the fact that the break in the rms amplitude versus energy relation is consistent with being the same for all QPO frequencies

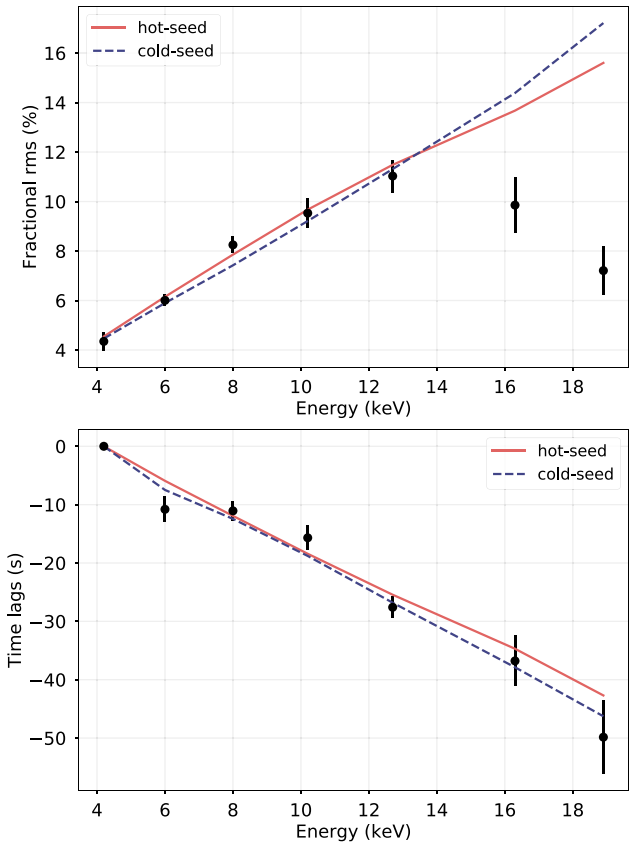

Figure 10. Modelling of the rms and time-lag spectra using the model of Kumar & Misra (2014). The solid red line represents the hot-seed photons model, and the dashed blue line represents the cold-seed photons model. (A colour version of this figure is available in the on-line version of the paper).

whereas the electron temperature of the corona changes as the QPO frequency changes (Ribeiro et al. 2017) makes it hard to establish a clear connection between E_b and kT_e. The presence of the break seems to be important, however, for the modelling of the radiative mechanism that produces the lower kHz QPO, as we discuss next.

4.5 The kHz QPOs as oscillations of the Comptonized flux

We used the model of Kumar & Misra (2014; see also Lee et al. 2001) to describe the relation of the rms amplitude with energy for the lower kHz QPO. The model of Kumar & Misra (2014) has as parameters: the amplitude of the oscillation of the external heating rate, $\delta H_{\rm ext}$, where the external heating rate is necessary to balance the cooling effect of inverse Compton scattering, the size of the Comptonizing medium, L, a parameter that describes the fraction of scattered photons that return to the source of seed photons, or feedback parameter,η, the temperature of the seed photon source, kT_s, the electron temperature of the Comptonizing medium, kT_e, and the optical depth of the Comptonizing medium, τ. Given that our rms spectra has only seven data points and the model requires six parameters, we also used the time-lag spectra presented by de Avellar et al. (2013), given that the model predicts both the rms and the lag spectrum. Furthermore, since the model cannot reproduce the break in the rms spectrum at high energies (see Kumar & Misra 2014, for a discussion about the possible reasons for this), we ignored the last two energy bins in our spectra during the fits.

Since the implementation of a fitting method for the model is computationally expensive, we leave that, together with a detailed exploration of the parameter space, for a subsequent paper (Karpouzas et al. in prep.); here, instead, we tested a set of model parameters and provide an approximate fit to both the rms and lag spectra simultaneously. According to Kumar & Misra (2016) the model is degenerate, and one can qualitatively fit the data using either a hot- or a cold-seed photon source. We find the same in this case, as shown in Fig. 10: This Figure shows a hot-seed model with $L = 1.18$ km, $\delta H_{\rm ext} = 0.08$, $\eta = 0.9$, $kT_e = 4.6$ keV, $kT_s = 1.3$ keV, and $\tau = 2.7$, and a cold-seed model with $L = 4.3$ km, $\delta H_{\rm ext} = 0.09$, $\eta = 0.6$, $kT_e = 3.8$ keV, $kT_s = 0.4$ keV, and $\tau = 10.4$.

5 CONCLUSION

The kHz QPOs in LMXB are likely a result of the interplay between different components in the accretion flow in these systems. We presented a study of the rms amplitude of the kHz QPOs in 4U 1636−53 in the frequency and energy domain, using the full set of archival observations of this source with the *RXTE* satellite. We find that the frequency of the kHz QPOs does not depend on photon energy whereas its amplitude does, reinforcing the idea that there are at least two distinctive mechanism responsible for the QPOs: a dynamical mechanism that sets the frequency and a radiative mechanism that sets the amplitude. We also show that the rms amplitude of the lower kHz QPO of 4U 1636−53 drops at high energies, which gives us a clue about the nature of the radiative mechanism behind this QPO.

We showed, for the first time for any source of kHz QPOs, the relation of rms amplitude of the kHz QPOs versus QPO frequency as a function of photon energy and QPO frequency. Our results give a more complete picture of these oscillations in the spectral-timing domain. This work helps to pave the way for current and future instruments such as NICER, ASTROSAT, HXMT, eXTP and Athena, the development of new techniques and tools for spectral-timing analysis (e.g. Huppenkothen et al. 2019), and the developments of new theoretical models to shed new light upon the nature of the kHz QPOs.

ACKNOWLEDGEMENTS

EMR acknowledges the support from Conselho Nacional de Desenvolvimento Científico e Tecnológico (CNPq — Brazil). MGBA acknowledges CNPq project 150999/2018-6 and The São Paulo Research Foundation (FAPESP — Brazil) Thematic Project 2013/26258-4. GB acknowledges funding support from the National Natural Science Foundation of China (NSFC) under grant numbers U1838116 and the CAS Pioneer Hundred Talent Program Y7CZ181002. This research has made use of data obtained from the High Energy Astrophysics Science Archive Research Center, provided by NASA's Goddard Space Flight Center.

REFERENCES

Altamirano D., van der Klis M., Méndez M., Jonker P. G., Klein-Wolt M., Lewin W. H. G., 2008, ApJ, 685, 436
Arnaud K. A., 1996, in Jacoby G. H., Barnes J., eds, ASP Conf. Ser. Vol. 101, Astronomical Data Analysis Software and Systems V. Astron. Soc. Pac., San Francisco, p. 17
Barret D., 2001, Adv. Space Res., 28, 307
Barret D., 2013, ApJ, 770, 9
Barret D., Olive J.-F., Miller M. C., 2005, MNRAS, 361, 855

Barret D., Olive J.-F., Miller M. C., 2006, MNRAS, 370, 1140
Belloni T., Méndez M., Homan J., 2005, A&A, 437, 209
Belloni T., Homan J., Motta S., Ratti E., Méndez M., 2007, MNRAS, 379, 247
Belloni T. M., Altamirano D., 2013, MNRAS, 432, 10
Berger M. et al., 1996, ApJ, 469, L13
Cackett E. M., 2016, ApJ, 826, 103
de Avellar M. G. B., Méndez M., Sanna A., Horvath J. E., 2013, MNRAS, 433, 3453
de Avellar M. G. B., Méndez M., Altamirano D., Sanna A., Zhang G., 2016, MNRAS, 461, 79
de Avellar M. G. B., Porth O., Younsi Z., Rezzolla L., 2018, MNRAS, 474, 3967
Di Salvo T., Méndez M., van der Klis M., Ford E., Robba N. R., 2001, ApJ, 546, 1107
Erkut M. H., Psaltis D., Alpar M. A., 2008, ApJ, 687, 1220
Gilfanov M., Revnivtsev M., Molkov S., 2003, A&A, 410, 217
Huang Y. et al., 2018, ApJ, 866, 122
Huppenkothen D. et al., 2019, J. Open Source Softw., 4, 1393
Kato S., 2005, PASJ, 57, 699
Kato S., 2009, PASJ, 61, 1237
Kluzniak W., Abramowicz M. A., 2001, preprint (astro-ph/0105057)
Kluzniak W., Michelson P., Wagoner R. V., 1990, ApJ, 358, 538
Kumar N., Misra R., 2014, MNRAS, 445, 2818
Kumar N., Misra R., 2016, MNRAS, 461, 4146
Lee H. C., Miller G. S., 1998, MNRAS, 299, 479
Lee H. C., Misra R., Taam R. E., 2001, ApJ, 549, L229
Lin D., Remillard R. A., Homan J., 2007, ApJ, 667, 1073
Lin Y.-F., Boutelier M., Barret D., Zhang S.-N., 2011, ApJ, 726, 74
Li X.-D., Zhang C.-M., 2005, ApJ, 635, L57
Lyu M., Méndez M., Altamirano D., 2014, MNRAS, 445, 3659
Méndez M., 2006, MNRAS, 371, 1925
Méndez M. et al., 1998a, ApJ, 494, L65
Mendez M., van der Klis M., Ford E. C., Wijnands R., van Paradijs J., 1998b, ApJ, 511, L49
Méndez M., van der Klis M., Ford E. C., 2001, ApJ, 561, 1016
Miller M. C., Lamb F. K., Psaltis D., 1998, ApJ, 508, 791
Morsink S. M., Stella L., 1999, ApJ, 513, 827
Mukherjee A., Bhattacharyya S., 2012, ApJ, 756, 55
Mukhopadhyay B., 2009, ApJ, 694, 387
Osherovich V., Titarchuk L., 1999, ApJ, 522, L113
Peille P., Barret D., Uttley P., 2015, ApJ, 811, 109
Ribeiro E. M., Méndez M., Zhang G., Sanna A., 2017, MNRAS, 471, 1208
Sanna A. et al., 2010, MNRAS, 408, 622
Sanna A., Méndez M., Belloni T., Altamirano D., 2012, MNRAS, 424, 2936
Sanna A., Hiemstra B., Méndez M., Altamirano D., Belloni T., Linares M., 2013, MNRAS, 432, 1144
Shi C., Li X.-D., 2009, MNRAS, 392, 264
Stella L., Vietri M., 1998, ApJ, 492, L59
Stella L., Vietri M., 1999, Phys. Rev. Lett., 82, 17
Strohmayer T. E., Zhang W., Swank J. H., Smale A., Titarchuk L., Day C., Lee U., 1996, ApJ, 469, L9
Titarchuk L., 2003, ApJ, 591, 354
Troyer J. S., Cackett E. M., Peille P., Barret D., 2018, ApJ, 860, 167
van der Klis M., Swank J. H., Zhang W., Jahoda K., Morgan E. H., Lewin W. H. G., Vaughan B., van Paradijs J., 1996, ApJ, 469, L1
van Doesburgh M., van der Klis M., Morsink S. M., 2018, MNRAS, 479, 426
van Straaten S., van der Klis M., di Salvo T., Belloni T., 2002, ApJ, 568, 912
Wang J., 2016, Int. J. Astron. Astrophys., 06, 82
Wijnands R. A. D., van der Klis M., van Paradijs J., Lewin W. H. G., Lamb F. K., Vaughan B., Kuulkers E., 1997, ApJ, 479, L141
Zhang C., 2004, A&A, 423, 401
Zhang W., Lapidus I., White N. E., Titarchuk L., 1996, ApJ, 469, L17
Zhang G., Méndez M., Sanna A., Ribeiro E. M., Gelfand J. D., 2017a, MNRAS, 465, 5003
Zhang L., Wang Y., Méndez M., Chen L., Qu J., Altamirano D., Belloni T., 2017b, ApJ, 845, 143

This paper has been typeset from a TEX/LATEX file prepared by the author.